J Mater Sci

Ceramics

High-throughput exploration of the Na_2O-ZrO_2-SiO_2-P_2O_5 composition space using thin film material libraries

A. Mockute[1,*] and A. Ludwig[1]

[1] *Chair for Materials Discovery and Interfaces, Institute for Materials, Faculty of Mechanical Engineering, Ruhr-University Bochum, Universitätsstraße 150, 44780 Bochum, Germany*

Received: 12 June 2024
Accepted: 9 September 2024

ABSTRACT

The composition space Na_2O-ZrO_2-SiO_2-P_2O_5 was explored using thin film material libraries and high-throughput characterization methods. The combinatorial synthesis comprised non-reactive magnetron co-sputtering at room temperature from two elemental targets Zr and Si, and a compound Na_3PO_4 target followed by a two-step annealing process. The NASICON phase formed for all compositions on the material library produced at the optimized deposition parameters, also displaying a phase-pure $Na_{1+x}Zr_2Si_xP_{3-x}O_{12}$ ($x = 0.4$—2.9) region. Analytical TEM analysis of the NASICON phase at a measurement area with stoichiometric composition revealed a fine-grained microstructure and homogeneous Si distribution, in contrast to Na-P excess conditions, where large Si-free NASICON grains have formed.

Introduction

The global energy demand is ever increasing and is projected to rise nearly 50% by 2050 [1]. In the view of the current climate crisis, energy harvesting inevitably steers toward environmentally conscious sources [2]. However, this type of energy supply is inherently fluctuating and often depends on multiple environmental factors such as season and weather conditions. Effective and reliable storage of the energy captured during the peak production time for later use is therefore crucial. Time separation of the energy production and energy consumption stages is enabled through battery technologies, where solid-state batteries are of particular interest due to improved safety and higher energy density compared to their liquid state counterparts. To date, solid-state batteries based on Li have been investigated most extensively and dominate the global market since their commercialization in 1991, the current development mainly driven by electric vehicle adoption. However, recent studies on resource assessment modeling predict that the global expansion of the electric vehicles fleet powered by Li ion batteries appears to be unrealistic due to geographically concentrated and finite Li supplies being the limiting factor [3, 4]. An

Handling Editor: David Cann.

Address correspondence to E-mail: aurelija.mockute@rub.de

https://doi.org/10.1007/s10853-024-10221-6
Published online: 19 September 2024

emerging alternative pathway for the next-generation solid-state batteries could be Li replacement with another alkaline metal: Na [5, 6]. In contrast to Li, Na is an abundant, geographically evenly distributed, and inexpensive element. Development of a suitable well-performing electrolyte is the current focus in advancing Na-based solid-state batteries. The solid-state electrolyte NASICON (Na super-ionic conductor) type materials attracted specific attention due to high ion-conductivity resulting from fast diffusion of Na ions within a three-dimensionally interconnected interstitial sites network in the crystal lattice [7]. $Na_{1+x}Zr_2Si_xP_{3-x}O_{12}$ in particular has been explored, owing to the combination of superior ion-conductivity and excellent electrochemical stability [8]. To date, most research on NASICON materials has been done employing bulk synthesis methods. Thin film solid-state batteries, on the other hand, allow manufacturing of miniaturized devices for use, e.g., in medical monitoring, biosensors, and wearable electronics [9]. Magnetron sputtering of NASICON thin films within the composition space Na_2O-SiO_2-P_2O_5-ZrO_2 was investigated in a series of publications by Horwat et al. Reactive sputtering from a single $Na_3Zr_2Si_2PO_{12}$ and composite $Na_3PO_4/ZrSiO_4$ targets in an Ar/O_2 mixture suffered from target instabilities such as cracking and Na ion migration or resulted in chemically heterogeneous films, respectively [10]. The film quality could be improved by reactive co-sputtering of Na_3PO_4 and $Zr_{0.52}Si_{0.48}$ alloy targets [11–13]. Room temperature (RT) deposition followed by annealing in air at 700 °C was used to transform amorphous films into crystalline NASICON phase [11–14].

In this study, we increase process flexibility through using elemental Zr and Si targets in combination with a Na_3PO_4 target and employ high-throughput characterization methods to explore the Na_2O-ZrO_2-SiO_2-P_2O_5 composition space, realized in form of thin film material libraries with focus on composition gradients of the $Na_{1+x}Zr_2Si_xP_{3-x}O_{12}$ NASICON phase.

Materials and methods

NASICON thin film material libraries (MLs) were synthesized by magnetron co-sputtering in confocal geometry from two 50 mm diameter commercial compound Na_3PO_4 (99.5% purity) and elemental Zr (99.99% purity) targets and one 100 mm diameter Si (99.999% purity) target in a high vacuum sputter system (Creavac GmbH, Germany). Na_3PO_4 was sputtered using radio frequency (RF), and Zr and Si using direct current (DC) power sources in power-controlled mode at 40 W, 26 W, and 7 W, respectively. In order to account for the substantially different sputter rates of the target materials, the lowest possible powers were set for Zr and Si in combination with a relatively high power for Na_3PO_4, taking the ceramic target susceptibility to thermal shock into account. In addition, the standard sputter chamber configuration was modified to further enhance the Na and P fluxes arriving to the substrate by lowering the substrate to the target-substrate distance of 8 cm and horizontal translation toward the Na_3PO_4 target. The depositions were carried out on 100 mm diameter single crystal $Al_2O_3(0001)$ wafers for 3 h at RT. Before depositions, the sputter chamber was evacuated to a base pressure of 1.1×10^{-5} Pa. The depositions were performed at 2 Pa pressure maintained with a 6N grade Ar (99.999%) flow of 50 sccm. Prior to the depositions, the substrates were cleaned in acetone and isopropanol ultrasonic baths for 5 min each. Al_2O_3 was selected as a non-reactive substrate stable at high processing temperatures.

As-deposited MLs were post-treated in two steps. First, they were annealed in the deposition chamber at 460 °C in O_2 at 100 Pa and 10 sccm flow for 1 h, followed by a second annealing in an air furnace at 900 °C for 1 h. Images of as-deposited and post-treated MLs were taken using an in-house built photo setup [15].

A high-throughput approach was implemented for investigations of the thin film libraries [16]. X-ray diffraction (XRD) and energy-dispersive X-ray spectroscopy (EDX) characterization was conducted in automated mode on a regular grid defining 342 individual measurement areas (MAs) with edge lengths of 4.5 mm × 4.5 mm. The numbering of the MAs starts with MA1 in the lower left corner of the ML. Symmetric θ-2θ XRD measurements were performed with a Bruker D8 Discover diffractometer equipped with a Cu Kα (λ = 0.154 nm) IμS microfocus source (collimated to a 1 mm point focus) and a VÅNTEC-500 area detector. A 2θ range from 5° to 60° was covered by collecting two frames for 30 s each at 2θ of 20° and 40°. The resultant two-dimensional (2D) frames were integrated into one-dimensional (1D) data sets using a DIFFRAC.EVA (Bruker) software. A Python script was implemented to automate the

conversion process. Elemental composition maps were obtained using a JEOL 5800 scanning electron microscopy (SEM) system. The EDX spectra were collected for 40 s at 20 kV acceleration voltage and 10 mm working distance. The data analysis was performed implementing a standard ZAF correction process provided by the INCA Energy software (Oxford Instruments). The surface morphologies were examined using a JEOL JSM-7200F SEM equipped with an EDX detector for correlative composition analysis.

Based on the XRD and EDX results, specific MAs were identified for further investigation with transmission electron microscopy (TEM). Cross-sectional samples for TEM analysis were prepared by standard focused ion beam (FIB) milling in FEI Helios G4 CX dual-beam system operated at 30 kV using a Ga ion beam. Prior to the FIB processing, the samples were coated with a ~ 70 nm Au layer to avoid excessive charging and minimize the ion beam damage. Due to general electron and ion beam sensitivity of NASION-type materials, thicker FIB lamellas than the standard thickness (typically ≤ 100 nm) were prepared. TEM images were recorded using a JEOL JEM ARM200F Cs-probe corrected TEM operated at 200 kV.

Results

Figure 1 shows photographs of the as-deposited and post-treated ML. The as-deposited film appears in brown–yellow color and is transparent. The region closest to the Zr target displays the most contrast. After the first annealing at 460 °C for 1 h in O_2, this contrast has reduced, but the ML still retained the brown–yellow color. The second annealing at 900 °C for 1 h in air resulted in complete color loss and film transformation into a transparent state. Photos of the ML were taken against a patterned background representing a grid of 342 MAs. Additionally, a black background was used for the photo after the second annealing to enhance the optical contrast. Three regions along the Zr-Na/P gradient, distinct in terms of color and surface roughness, can be distinguished on the ML in the final state, denoted as *A*, *B*, and *C* in Fig. 1.

EDX elemental maps of Na, P, Si, and Zr in the final state of the ML, i.e., after the second annealing, are presented in Fig. 2. Oxygen signal was recorded and included into the data analysis, but not quantified due to superposition with a much stronger O peak originating from the Al_2O_3 substrate. With the four elements Na, P, Si, and Zr used in quantification, the covered composition ranges are 11–61 at. %, 0–48 at. %, 1–52 at. %, and 3–80 at. %, respectively. MAs with the targeted composition $Na_{1+x}Zr_2Si_xP_{3-x}O_{12}$, with $0 \le x \le 3$, are highlighted in Fig. 2b. In Fig. 2c, ± 5 at. % deviation of x is allowed, in order to also include over- and under-stoichiometric NASICON compositions. The sputter powers on the individual targets were adjusted to ensure that the region of the aimed NASICON compositions would be located in the central part of the ML, thus taking full advantage of the composition gradients in the NASICON phase as well as elucidating on the competing phases forming alongside the NASICON phase at off-stoichiometric conditions in the surrounding regions. MA166, located in region *B*, represents a stoichiometric NASICON

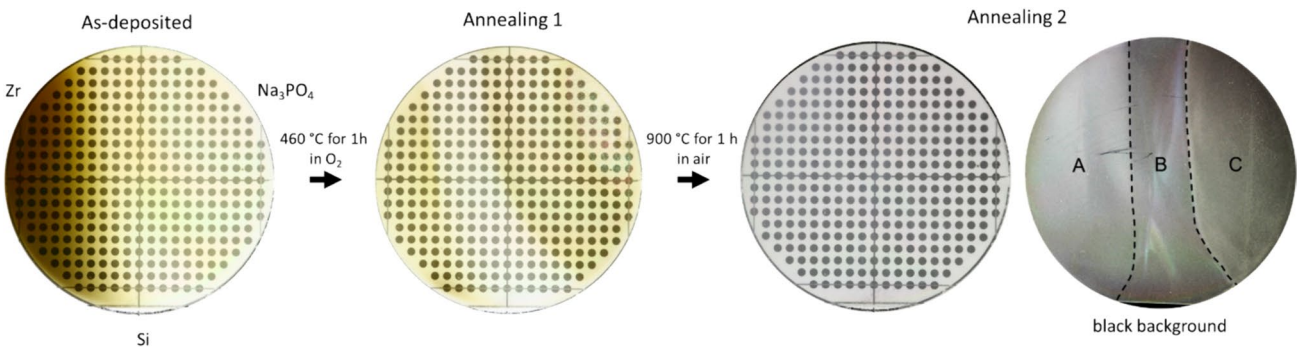

Figure 1 Photographs of as-deposited and subsequently annealed ML along with the target configuration relative to the substrate. Black background was used to enhance the contrast and reveal three optically distinct regions which developed after the second annealing, marked as *A*, *B*, and *C*.

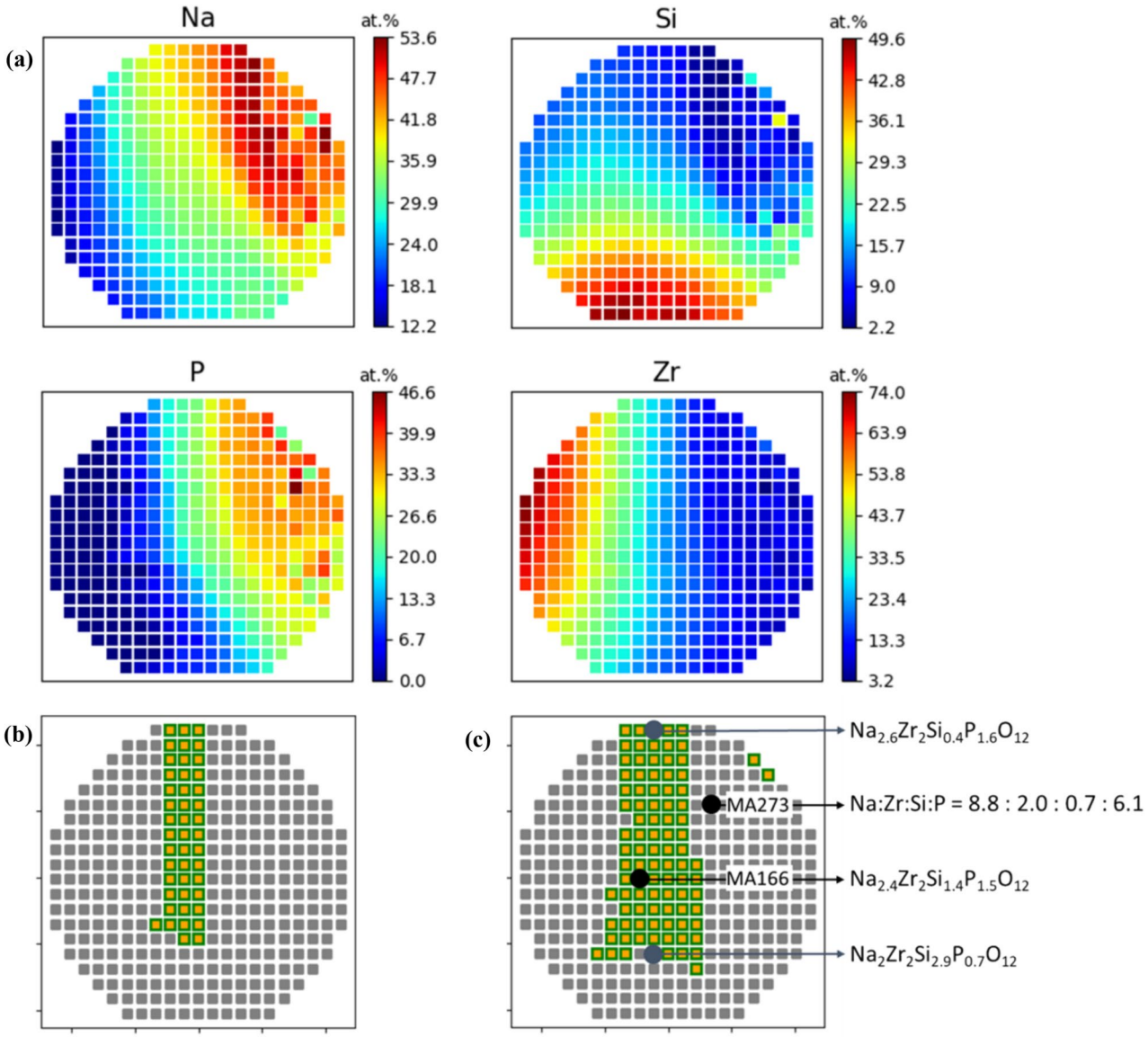

Figure 2 EDX of the ML in its final state after the second annealing. **a** Elemental maps of Na, P, Si, and Zr along with MAs corresponding to $Na_{1+x}Zr_2Si_xP_{3-x}O_{12}$ composition with **b** $0 \leq x \leq 3$ and **c** allowing ± 5 at. % deviation in order to account for over- and under-stoichiometry. End compositions along the Si gradient as well as compositions of MA166 and MA273 selected for further TEM analysis are also indicated.

composition of $Na_{2.4}Zr_2Si_{1.4}P_{1.5}O_{12}$ and, together with MA273 from region *C*, has been selected for further TEM analysis. The compositions of the MAs indicated in Fig. 2c are normalized by Zr = 2 and assume stoichiometric occupancy of O.

The previously discussed formation of the three distinct optical regions developed on the ML after the second annealing can be correlated to the elemental EDX maps in Fig. 2a. The region *A* coincides with the highest Zr content, while the region *C* can be related to the highest contents of Na and P. The region *B* located in-between corresponds exactly to the NASICON compositions, as shown in Fig. 2b, except for the lower part closest to the Si target and the resultant oversupply of Si.

XRD measurements carried out on a few selected MAs (close to each target and in the center of the ML) after the first annealing indicated amorphous material. After the second annealing, full XRD mapping has been performed. Each of the three optically distinct

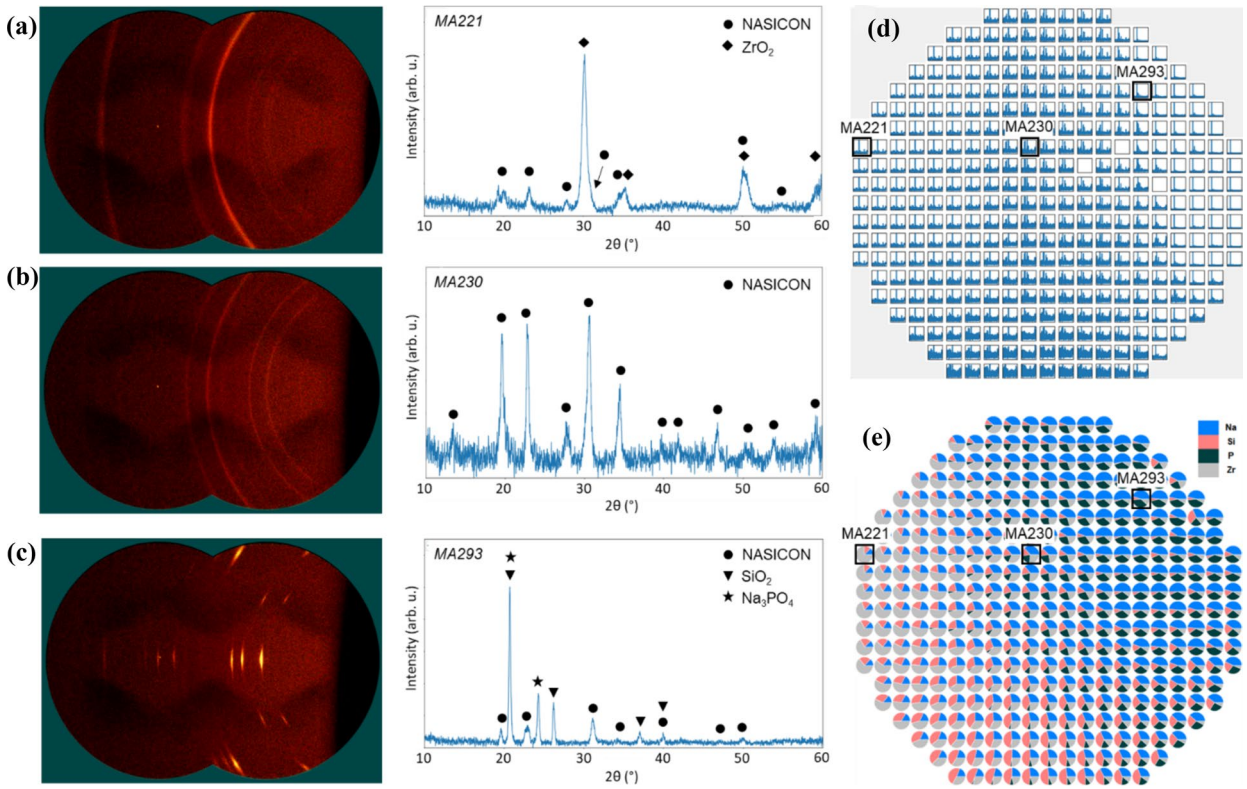

Figure 3 Representative 2D XRD along with the integrated patterns obtain from the regions **a** *A (MA221)*, **b** *B (MA230)*, and **c** *C (MA293)* with the selected MAs marked in **d** the XRD overview map and **e** EDX pie-chart diagram indicating the relative elemental compositions of Na, Zr, Si, and P at each of the 342 MAs in the final state of the ML.

regions *A*, *B*, and *C* displays a characteristic XRD pattern, shown in Fig. 3. In region *A*, the main phase is cubic ZrO_2 (ICSD-36700), although some NASICON phase (ICSD-473) has also formed. In region *B*, exclusively NASICON phase was detected. The NASICON peaks have grown in intensity and exhibit narrower peak widths, indicating larger crystallite sizes. Full diffraction rings observed in 2D XRD patterns in both regions *A* and *B* reveal the polycrystalline nature of the film. In contrast, in region *C* the NASICON phase develops preferential texture. Furthermore, formation of SiO_2 (ICSD-41412) and Na_3PO_4 (ICSD-91565) in the region *C* can also be concluded. Figure 3e and d shows the correlation between the phase distribution on the ML and the EDX composition gradient. ZrO_2 is the dominant phase in the Zr-rich region, while Na_3PO_4 emerges in Na and P excess conditions. Presence of SiO_2 is a consequence of no Si being incorporated in the textured NASICON phase in region *C*, as revealed by TEM–EDX analysis. In the central region *B*, the relative elemental contents are in correct proportions to support formation of phase-pure NASICON film, except for the Si-rich part closest to the Si target.

Surface morphologies of the two selected MAs from representative NASICON regions *B* and *C* are compared in Fig. 4. MA166 exhibits fine surface roughness with occasional surface cracks up to 4 μm in length. SEM imaging induced significant electron beam damage, particularly in MA166. An example of a post-imaged area is shown as an inset in Fig. 4a. The film has swelled forming surface bubbles, some associated with protruding metallic Na features (as determined by correlative EDX) preferentially forming at the perimeter of the investigated area. Solid electrolytes are typically sensitive to electron and ion beams due to high mobility of ions under the influence of electric fields, resulting in structural and composition alterations [17]. Relating to a textured 2D XRD, MA273 displays a distinctively different surface with grain outlines clearly visible. The film is composed of well-distinguished individual irregular hexagonal shape platelet-like grains up to 10 μm in

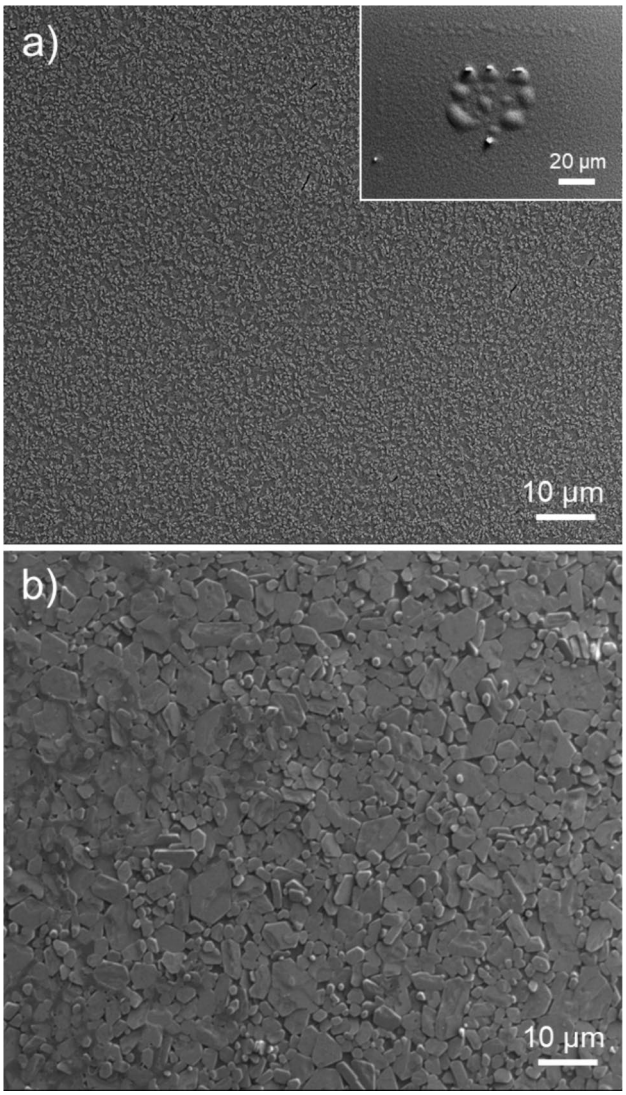

Figure 4 SEM surface overview images of **a** MA166 and **b** MA273. The inset in **a** illustrates swelling of the film and formation of metallic Na features (bright contrast) caused by electron beam damage for the imaged area.

width, preferentially oriented with the flat facet lying parallel to the surface.

Overview TEM images of MA166 and MA273 are shown in Fig. 5. Both coatings are dense and well adherent to the substrate. As concluded from SEM, microstructures composed of fine randomly oriented grains versus preferentially textured large platelet-like grains are revealed in cross section for MA166 and MA273, respectively. The film thickness is 500 nm for MA166 and 975 nm for MA273, a difference which is to be expected on a ML with composition gradients and related thickness

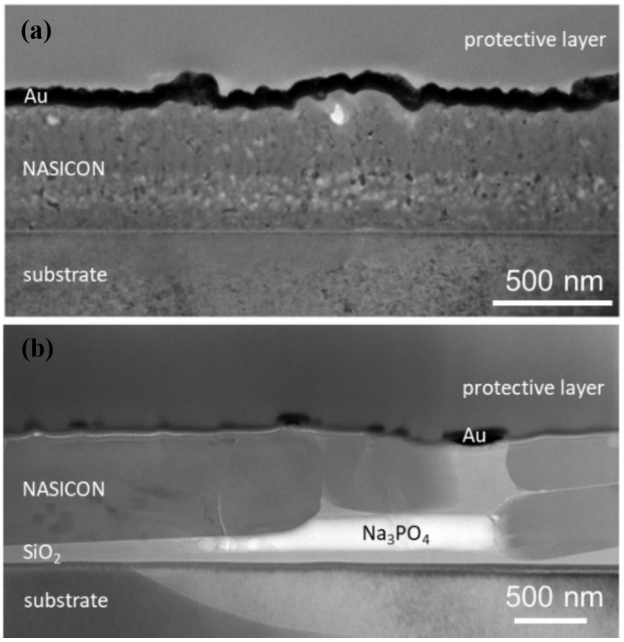

Figure 5 TEM cross-section overview images of **a** MA166 and **b** MA273.

gradients. The thickness of the large grains in MA273 measures up to 810 nm, i.e., a single grain may extend almost throughout the entire film thickness. The black layer on top of the film in MA166 is a protective Au layer, which has been partially removed in MA273 during FIB sample preparation. The layered contrast within the film in MA166 arises from the deposition process which was interrupted mid-way.

Qualitative scanning (S)TEM–EDX maps in Fig. 6 show the constituting elements and their distribution in the films. In accordance with literature [17], even though the film structural integrity has been retained, FIB sample preparation with Ga ion beam led to severe Na loss as compared with SEM–EDX results, including Na ion migration into the protective carbon layer. The major qualitative difference between the two MAs is Si incorporation into the NASICON films. In MA166 Si is homogeneously distributed throughout the NASICON film with no signs of other Si-containing phases in neither (S)TEM–EDX elemental maps nor XRD. In contrast, the NASICON grains in MA273 comprise Na-Zr-P-O. Si is not accommodated in the NASICON structure and accumulates as SiO_2 into a continuous ~ 66 nm layer at the film/substrate interface as well as in the

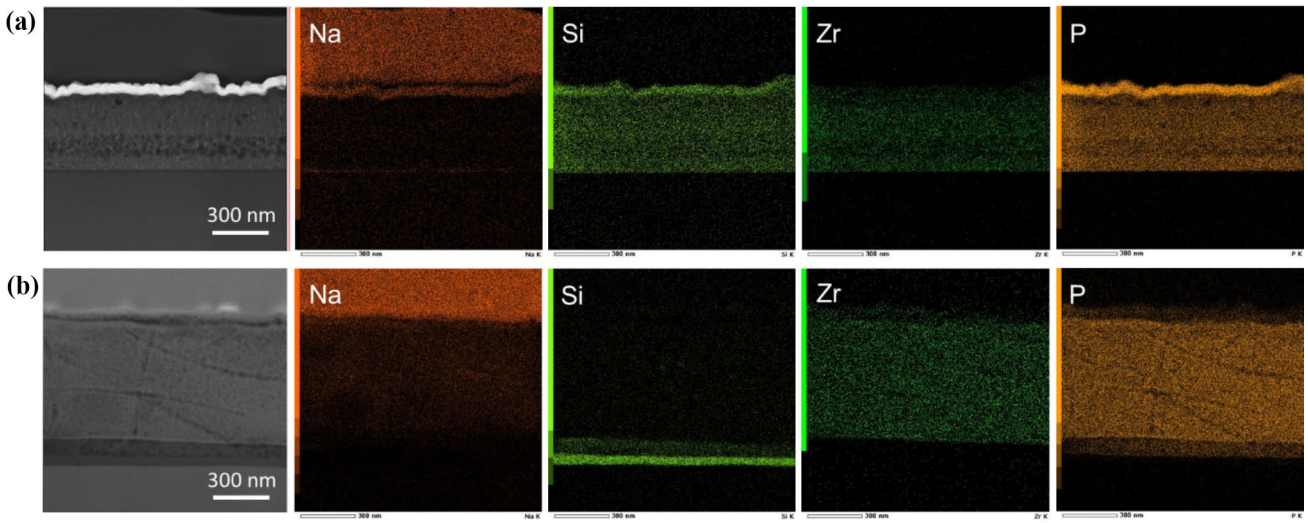

Figure 6 Qualitative (S)TEM–EDX maps showing constituent elements of the NASICON phase in **a** MA166 and **b** MA273.

spaces between the grains. The grain displaying the brightest contrast in Fig. 5b MA273 is Na- and P-rich, which, taking into account ~ 60% Na loss during standard RT FIB sample preparation [17], is in agreement with the composition of Na_3PO_4 phase identified in XRD.

Discussion

With the aim to improve the process flexibility and explore large compositional ranges, we performed combinatorial depositions using Zr and Si elemental targets instead of both elements contained in a Zr-Si alloy target, as was the case in all previous Na_2O-ZrO_2-SiO_2-P_2O_5 thin film studies [11–14]. A Na_3PO_4 compound target was used as a source for both Na and P, which resulted in a fixed Na : P ratio throughout the ML and, consequently, attainable stoichiometric NASICON compositions falling into a certain predefined range. However, separating Na and P into elemental sputtering targets is not feasible for a magnetron sputtering process.

In addition to standard structure and composition characterization with XRD and EDX, we present TEM analysis complimented with qualitative EDX elemental maps of $Na_{1+x}Zr_2Si_xP_{3-x}O_{12}$ thin films. Precautions have been taken against ion and electron beam exposure damage during FIB sample preparation, TEM imaging, and (S)TEM–EDX spectra acquisition; however, some progressive damage of the films has still occurred. Even though quantitative (S)TEM–EDX evaluation could not be performed due to severe Na loss, qualitative observations still illustrate the importance of local composition analysis of individual grains, as opposed to relying solely on the global composition and phase constitution characterization methods. Here, (S)TEM–EDX reveals difference in the constituting elements, Si specifically, of the NASICON phase formed in two separate regions on the ML. This is of importance due profound Si effect on $Na_{1+x}Zr_2Si_xP_{3-x}O_{12}$ performance as solid-state electrolyte and could otherwise not be concluded based on XRD and SEM–EDX results alone.

The difference between the two investigated MAs in terms of Si accommodation within the NASICON structure may relate to their respective elemental compositions. Si : P ratio at MA273 is 1 : 8.7, while almost equal Si and P fluxes arrive at MA166. In the $Na_{1+x}Zr_2Si_xP_{3-x}O_{12}$ structure, Si and P share the same site on the crystal lattice. P being in oversupply in MA273 may act as the preferred element for the shared site, while the little amount of available Si is expelled to the grain boundaries.

Conclusions

The composition space Na_2O-ZrO_2-SiO_2-P_2O_5 was explored using co-sputtered thin film MLs with focus on formation of compounds with stoichiometry $Na_{1+x}Zr_2Si_xP_{3-x}O_{12}$. The NASICON phase was

observed for all compositions synthesized using optimized conditions, displaying a phase-pure region in the central part of the ML. Closest to Zr and Na_3PO_4 targets, the phases ZrO_2 and Na_3PO_4 were also present, respectively. The film microstructure and Si incorporation into the NASICON phase were strongly influenced by the incoming elemental fluxes. The phase-pure NASICON region in the central part of the ML consists of fine grains and covers a Si gradient of $x = 0.4—2.9$. In contrast, Na-P excess conditions lead to formation of large textured Si-free NASICON grains.

Conflicts of interest

The authors declare no conflict of interest.

Acknowledgements

This work was funded by Mercator Research Center Ruhr (MERCUR), project number Pr-2019-0042 (Novel NASICON-type sodium solid electrolytes for next-generation sodium ion batteries). Center for Interface-Dominated High-Performance Materials (ZGH) at Ruhr-University Bochum is acknowledged for the use of XRD, SEM, FIB, and TEM. We thank Dr. Aleksander Kostka for support with (S)TEM-EDX measurements.

Author contributions

Aurelija Mockute contributed to investigation, visualization, and writing—original draft preparation. Alfred Ludwig was involved in conceptualization, funding acquisition, and writing—reviewing and editing.

Funding

Open Access funding enabled and organized by Projekt DEAL. Mercator Research Center Ruhr, Pr-2019-0042, Alfred Ludwig.

Data availability

The data that support the findings of this study are available from the corresponding author upon reasonable request.

References

[1] International Energy Agency (2021), World Energy Outlook 2021, IEA

[2] Gielen D, Boshell F, Saygin D, Bazilian MD, Wagner N, Gorini R (2019) The role of renewable energy in the global energy transformation. Energ Strat Rev 24(6):38–50. https://doi.org/10.1016/j.esr.2019.01.006

[3] Sanginesi F, Millacci G, Giaccherini A, Buccianti A, Fusi L, Di Benedetto F, Pardi L (2023) Long term lithium availability and electric mobility: what can we learn from resource assessment? J Geochem Explor 249(10):107212. https://doi.org/10.1016/j.gexplo.2023.107212

[4] Greim P, Solomon AA, Breyer C (2020) Assessment of lithium criticality in the global energy transition and addressing policy gaps in transportation. Nat Commun 11(1):4570. https://doi.org/10.1038/s41467-020-18402-y

[5] Abraham KM (2020) How comparable are sodium-ion batteries to lithium-ion counterparts? ACS Energy Lett 5(11):3544–3547. https://doi.org/10.1021/acsenergylett.0c02181

[6] Rudola A, Sayers R, Wright CJ, Barker J (2023) Opportunities for moderate-range electric vehicles using

sustainable sodium-ion batteries. Nat Energy 8(3):215–218. https://doi.org/10.1038/s41560-023-01215-w

[7] Li C, Li R, Liu K, Si R, Zhang Z, Hu Y-S (2022) NaSICON: a promising solid electrolyte for solid-state sodium batteries. Interdisciplinary Materials 1(3):396–416. https://doi.org/10.1002/idm2.12044

[8] Zhang Z, Wenzel S, Zhu Y, Sann J, Shen L, Yang J, Yao X, Hu Y-S, Wolverton C, Li H, Chen L, Janek J (2020) $Na_3Zr_2Si_2PO_{12}$: a stable Na+ ion solid electrolyte for solid-state batteries. ACS Applied Energy Materials 3(8):7427–7437. https://doi.org/10.1021/acsaem.0c00820

[9] Wu T, Dai W, Ke M, Huang Q, Lu L (2021) All-solid-state thin film μ-batteries for microelectronics. Advanced Science 8(19):2100774. https://doi.org/10.1002/advs.202100774

[10] Horwat D, Pierson JF, Billard A (2007) Magnetron sputtering of NASICON ($Na_3Zr_2Si_2PO_{12}$) thin films Part I: limitations of the classical methods. Surf Coat Technol 201(16–17):7013–7017. https://doi.org/10.1016/j.surfcoat.2007.01.007

[11] Horwat D, Pierson JF, Billard A (2007) Magnetron sputtering of NASICON ($Na_3Zr_2Si_2PO_{12}$) thin films. Surf Coat Technol 201(16–17):7060–7065. https://doi.org/10.1016/j.surfcoat.2007.01.016

[12] Horwat D, Pierson JF, Billard A (2008) Towards a thin films electrochromic device using NASICON electrolyte. Ionics 14:227–233. https://doi.org/10.1007/s11581-007-0176-x

[13] Horwat D, Billard A (2005) Sodium superionic conductor putter-deposited coatings. Ionics 11:120–125

[14] Horwat D, Pierson JF, Billard A (2008) Structural-electrical-optical properties relationship of sodium superionic conductor sputter-deposited coatings. Thin Solid Films 516(10):3387–3393. https://doi.org/10.1016/j.tsf.2007.10.086

[15] Thienhaus S, Naujoks D, Pfetzing-Micklich J, König D, Ludwig A (2014) Rapid identification of areas of interest in thin film materials libraries by combining electrical, optical, X-ray diffraction, and mechanical high-throughput measurements: a case study for the system Ni-Al. ACS Comb Sci 16(12):686–694. https://doi.org/10.1021/co5000757

[16] Ludwig A (2019) Discovery of new materials using combinatorial synthesis and high-throughput characterization of thin-film materials libraries combined with computational methods. npj Comput Mater. https://doi.org/10.1038/s41524-019-0205-0

[17] Ding Z, Tang Y, Chakravadhanula VSK, Ma Q, Tietz F, Dai Y, Scherer T, Kübel C (2023) Exploring the influence of focused ion beam processing and scanning electron microscopy imaging on solid-state electrolytes. Microscopy 72(4):326–335. https://doi.org/10.1093/jmicro/dfac064